

Real-World Remote Sensing Image Dehazing: Benchmark and Baseline

Zeng-Hui Zhu[†], Wei Lu[†], Si-Bao Chen^{*}, Chris H. Q. Ding, Jin Tang, and Bin Luo

Abstract—Remote Sensing Image Dehazing (RSID) poses significant challenges in real-world scenarios due to the complex atmospheric conditions and severe color distortions that degrade image quality. The scarcity of real-world remote sensing hazy image pairs has compelled existing methods to rely primarily on synthetic datasets. However, these methods struggle with real-world applications due to the inherent domain gap between synthetic and real data. To address this, we introduce Real-World Remote Sensing Hazy Image Dataset (RRSHID), the first large-scale dataset featuring real-world hazy and dehazed image pairs across diverse atmospheric conditions. Based on this, we propose MCAF-Net, a novel framework tailored for real-world RSID. Its effectiveness arises from three innovative components: Multi-branch Feature Integration Block Aggregator (MFIBA), which enables robust feature extraction through cascaded integration blocks and parallel multi-branch processing; Color-Calibrated Self-Supervised Attention Module (CSAM), which mitigates complex color distortions via self-supervised learning and attention-guided refinement; and Multi-Scale Feature Adaptive Fusion Module (MFAFM), which integrates features effectively while preserving local details and global context. Extensive experiments validate that MCAF-Net demonstrates state-of-the-art performance in real-world RSID, while maintaining competitive performance on synthetic datasets. The introduction of RRSHID and MCAF-Net sets new benchmarks for real-world RSID research, advancing practical solutions for this complex task. The code and dataset are publicly available at [here](#).

Index Terms—Remote sensing, real-world dehazing, color calibration, multi-branch processing, adaptive fusion.

I. INTRODUCTION

REMOTE sensing (RS) imagery serves as a pivotal enabler for environmental sciences and agricultural applications, driving significant advancements in urban planning, agricultural monitoring, disaster management, and environmental conservation [1]–[6]. However, the ubiquitous presence of atmospheric haze presents a persistent obstacle, degrading image quality by diminishing contrast and obscuring fine

[†]Equal contribution: Zeng-Hui Zhu and Wei Lu. ^{*}Corresponding author: Si-Bao Chen. This work was supported in part by NSFC Key Project of International (Regional) Cooperation and Exchanges (No. 61860206004), NSFC Key Project of Joint Fund for Enterprise Innovation and Development (No. U20B2068, U24A20342) and National Natural Science Foundation of China (No. 61976004).

Zeng-Hui Zhu, Wei Lu, Si-Bao Chen, Jin Tang, and Bin Luo are with the MOE Key Laboratory of ICSP, IMIS Laboratory of Anhui, Anhui Provincial Key Laboratory of Multimodal Cognitive Computation, Zenmorn-AHU AI Joint Laboratory, School of Computer Science and Technology, Anhui University, Hefei 230601, China (e-mail: 1525074487@qq.com; 2858191255@qq.com; sbchen@ahu.edu.cn; tangjin@ahu.edu.cn; luobin@ahu.edu.cn).

Chris H. Q. Ding is with the School of Data Science (SDS), Chinese University of Hong Kong, Shenzhen 518172, China (e-mail: chrisding@cuhk.edu.cn).

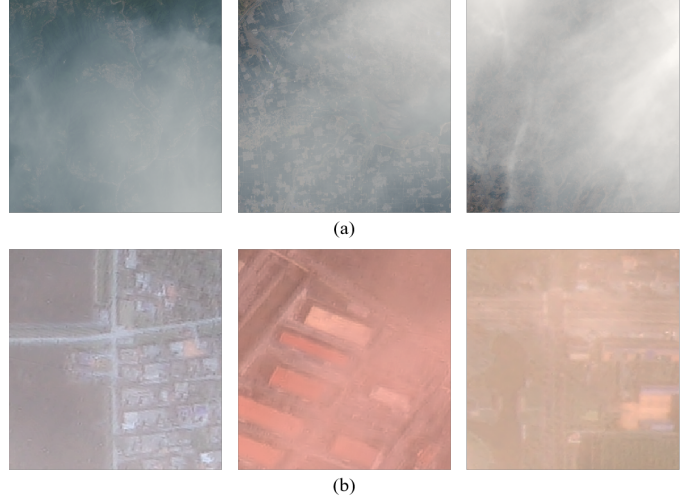


Fig. 1. Visual comparison of synthetic and real-world RS hazy images. (a) Synthetic hazy images from the RS-HAZE dataset [7]. (b) Real-world hazy images from our RRSHID dataset, highlighting complex color variations.

details. Such degradation severely compromises the precision and reliability of subsequent analytical tasks, underscoring the urgent need for efficient, robust dehazing algorithms tailored to practical RS applications.

In recent years, deep learning has catalyzed remarkable progress in RS image dehazing (RSID) [8]. Pioneering efforts such as TransWeather [9] introduced Transformer architectures to dehazing, while 4KDehazing [10] advanced high-resolution dehazing through sophisticated multi-scale feature extraction. These methods have predominantly been developed and validated on synthetic datasets like RICE [11] and RS-HAZE [7], achieving impressive results—e.g., FFA-Net [12] with a PSNR of 33.52 dB on RICE, and DehazeFormer [7] with 39.57 dB on RS-HAZE. However, when deployed on real-world RS hazy images, these models frequently suffer substantial performance drops. This gap arises from three critical challenges:

- 1) *Domain Discrepancy*: Synthetic datasets rely on simplified atmospheric scattering models [13], which inadequately represent the intricate, non-linear atmospheric dynamics of real-world scenes.
- 2) *Complex Atmospheric Variability*: Real-world RS imagery contends with altitude-dependent atmospheric effects and spatially heterogeneous haze distributions [14], which vary with elevation, time, and geography—conditions significantly more complex than those in synthetic data [7].
- 3) *Color Fidelity Challenges*: Color Fidelity Challenges: Real-world hazy images display pronounced color dis-

tortions caused by multiple scattering and sensor-specific responses [15], as shown in Fig. 1, in stark contrast to the basic color shifts observed in synthetic datasets.

To address these challenges, we introduce the Real-World Remote Sensing Hazy Image Dataset (RRSHID). It is the first large-scale dataset featuring real-world hazy and dehazed image pairs across diverse atmospheric conditions and geographical contexts. Its construction is detailed in Section IV.

With this dataset established, we propose the Multi-branch Color-calibrated Adaptive Fusion Network (MCAF-Net), which demonstrates state-of-the-art (SOTA) performance in real-world RSID challenges.

At its core, MCAF-Net utilizes the Multi-branch Feature Integration Block Aggregator (MFIBA) as its primary encoding component, consisting of three cascaded Multi-branch Feature Integration Blocks (MFIBs). Each MFIB splits input features into four parallel branches—height-width (hw), channel-height (ch), channel-width (cw), and point-wise integration—using a channel-splitting strategy [16]. Tailored convolution and adaptive parameters within each branch extract multi-scale, multi-dimensional feature representations, with grouped convolutions and parameter sharing ensuring computational efficiency. By cascading three MFIBs, MFIBA enhances feature robustness and regularizes information flow, adeptly balancing efficiency and representational capacity for real-world RSID.

Traditional RSID methods often adopt simplistic reconstruction techniques, such as direct feature mapping [17] or basic skip connections [18], neglecting the pivotal role of color calibration in real-world contexts. To address this, we introduce the Color-calibrated Self-supervised Attention Module (CSAM). CSAM combines self-supervised color learning with attention-driven refinement via two mechanisms: (1) an intermediate "fake image" generated through a learnable color correction matrix for implicit color supervision, and (2) a query-key-value attention mechanism where color-calibrated features guide refinement through a global channel attention branch (for broad color consistency, e.g., sky regions) and a local depth-wise convolution branch (for detail preservation, e.g., urban edges). Tailored for RSID and inspired by recent restoration advances [19], CSAM bridges encoding and decoding, ensuring both color accuracy and structural integrity.

Moreover, conventional feature fusion in RSID—often limited to 1×1 convolutions or selective kernel methods [7]—struggles with the spatial heterogeneity and scale-varying degradation of real-world haze. These approaches either oversimplify feature interactions or rely on static receptive fields, failing to capture spectral-spatial complexity. Our Multi-scale Feature Adaptive Fusion Module (MFAFM) overcomes these shortcomings by integrating features across scales and layers via a three-branch architecture (3×3 , 5×5 , 7×7 kernels). Dual attention—channel and spatial—prioritizes salient features, while residual learning and adaptive adjustments stabilize training and align features effectively. This design ensures adaptive, multi-scale fusion, preserving local details and global coherence critical for real-world RSID.

Our main contributions are summarized as follows:

- 1) *RRSHID*: The first real-world RS hazy image dataset, encompassing real-world hazy and dehazed image pairs,

fostering advancements in real-world RSID research.

- 2) *MCAF-Net*: A novel framework for real-world RSID, leveraging hierarchical feature refinement through specialized modules.
- 3) *MFIBA*: An efficient module for cross-dimensional feature integration via cascaded blocks and multi-branch processing, capturing haze-invariant patterns with computational efficiency.
- 4) *CSAM*: A color-calibration module addressing distortions and preserving details via self-supervised learning and attention-guided refinement.
- 5) *MFAFM*: An adaptive multi-scale fusion module preserving local details and global context for complex real-world scenarios.

II. RELATED WORK

A. Model-Based RSID

Model-based methods for RSID have historically leveraged physical models of atmospheric scattering to estimate and mitigate haze effects. Pioneering efforts, such as the Dark Channel Prior (DCP) [8], relied on the assumption that haze-free images contain dark pixels to derive transmission maps. However, this assumption often falters in RS scenarios due to expansive bright regions, such as deserts or snow-covered landscapes. To address this, subsequent innovations like the Haze-Lines Prior [20] exploited linear pixel relationships in hazy images, while the Color Attenuation Prior [21] utilized depth-color attenuation correlations to refine estimates. Despite these advancements, such methods frequently struggle to accommodate the diverse atmospheric conditions and intricate scene compositions prevalent in RS imagery. More recent developments, exemplified by Non-Local Image Dehazing [22], have integrated spatial context and global information to bolster performance. Nevertheless, model-based approaches remain challenged by varying atmospheric dynamics and the preservation of fine details in RS images.

B. Deep Learning-Based RSID

The advent of deep learning has transformed RSID, surpassing the limitations of traditional model-based techniques. Early contributions, such as DehazeNet [23] and MSCNN [24], pioneered convolutional neural networks (CNNs) for transmission map estimation, establishing a benchmark for superior performance. AOD-Net [25] advanced this paradigm by introducing end-to-end training for direct clean image recovery. DCPDN [26] further refined the approach by jointly optimizing transmission maps and atmospheric light within a cohesive framework. As the field matured, attention mechanisms and multi-scale architectures gained traction. FFA-Net [12] and GridDehazeNet [27] incorporated these features to effectively capture global context and local intricacies. PSMB-Net [28] extended this trajectory with dual-path feature interactions to tackle non-uniform haze in urban RS scenes, while MSBDN [29] introduced a boosted decoder for enhanced feature propagation. PSD-Net [30] employed pyramid supervision to enable progressive dehazing.

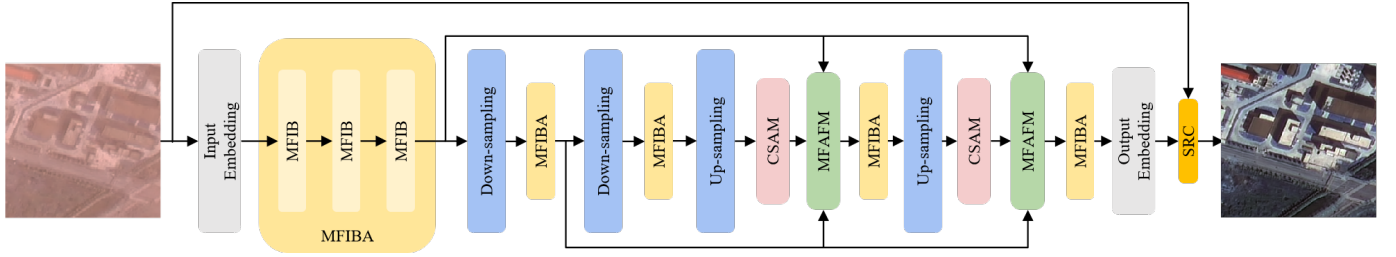


Fig. 2. The proposed MCAF-Net architecture. It adopts a U-shaped design for real-world RSID. The encoder utilizes the MFIBA with three cascaded MFIBAs, while the decoder integrates CSAM and MFAFM, creating a robust framework for real-world dehazing.

Recent innovations have shifted toward transformer-based architectures, marking a significant evolution in RSID. DehazeFormer [7] leveraged shifted window attention to model long-range dependencies, offering robust haze removal across complex scenes. PCSformer [31] built upon this by introducing cross-stripe attention modules to capture vertical and horizontal haze gradients, augmented by proxy tokens for computational efficiency. Trinity-Net [1] integrated gradient-guided Swin transformers with physics-informed priors, facilitating joint optimization of dehazing and downstream tasks, such as land cover classification.

To overcome data scarcity—a persistent challenge in RSID—hybrid learning strategies have emerged. SCANet [32] proposed a self-paced semi-curricular attention network, blending curriculum learning with channel-spatial attention to address non-homogeneous haze. Semi-supervised methods [33] harnessed both labeled and unlabeled data, while domain adaptation techniques [14] bridged synthetic and real-world domains. Self-supervised learning [34] has also shown promise in exploiting unlabeled RS data for improved dehazing. SF-SNiD [35] explored frequency-consistent twin fusion, while MaxDehazeNet [36] applied maximum flow theory to model atmospheric scattering, enhancing physical interpretability.

III. PROPOSED METHOD

In this section, we detail the architecture and key components of the proposed MCAF-Net, specifically engineered for RSID. As illustrated in Fig. 2, MCAF-Net employs a U-shaped architecture with five stages, integrating three novel modules: MFIBA, CSAM and MFAFM.

The encoder leverages MFIBA to perform efficient, cross-dimensional feature extraction through cascaded multi-branch processing, addressing the spatial heterogeneity of real-world haze. CSAM bridges the encoder and decoder by progressively refining color fidelity through attention-guided refinement, ensuring structural preservation. In the decoder, MFAFM adaptively fuses multi-scale features using dual attention mechanisms—channel attention for spectral recalibration and spatial attention for terrain-specific haze suppression—effectively balancing local details and global context. This design is tailored to tackle the complex atmospheric variability and color distortions prevalent in real-world RSID scenarios, outperforming conventional approaches reliant on static feature processing.

A. MFIBA

Conventional RSID methods uniformly process features across all dimensions, propagating redundant information that

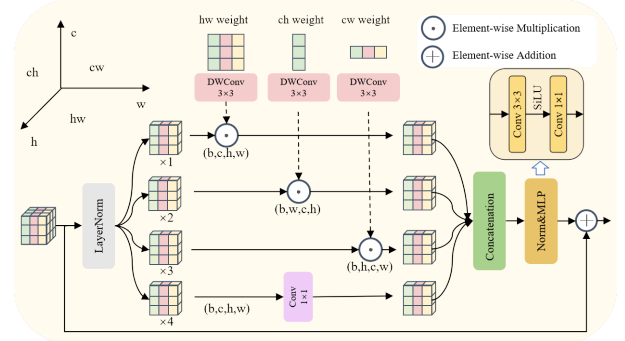


Fig. 3. Structure of the proposed MFIB. It employs axis-oriented attention to refine feature representation and flow, achieving superior dehazing performance with reduced computational overhead.

obscures critical structural details and degrades generalization in complex atmospheric conditions. Real-world RSID requires robust feature extraction capable of addressing spatially heterogeneous haze distributions, a challenge unmet by conventional methods reliant on static full-channel convolutions [12], [37]. To overcome this limitation, we propose the MFIBA, a lightweight module grounded in dynamic feature disentanglement theory [38]. MFIBA selectively amplifies haze-invariant features while suppressing noise, achieving a balance between computational efficiency and representational capacity tailored for real-world RSID.

MFIBA processes input features $\mathbf{X} \in \mathbb{R}^{b \times c \times h \times w}$ by partitioning them into four subgroups $\{x_1, x_2, x_3, x_4\}$, each with dimensions $(1, c/4, h, w)$. Three learnable queries— \mathbf{Q}_{hw} , \mathbf{Q}_{ch} and \mathbf{Q}_{cw} —are dynamically generated for the spatial (h - w), channel-height (c - h), and channel-width (c - w) dimensions. These queries, initialized using Xavier normal distribution [39], interact with reshaped feature groups via Hadamard products $\mathbf{Q}_{ij} \odot \mathbf{X}_{ij}$, selectively attenuating redundant haze patterns while preserving cross-dimensional correlations. A cascaded architecture with three MFIB stages progressively refines contextual representations through residual connections, expanding the effective receptive field to capture large-scale haze structures. Computational efficiency is achieved through depth-wise separable convolutions [40] and 1×1 channel interactions, reducing complexity from $\mathcal{O}(c^2 h w k^2)$ to $\mathcal{O}(c^2 h w / 4 + 3 c h w)$. This process is formalized as:

$$\begin{aligned}
 [X_{hw}, X_{ch}, X_{cw}, X_0] &= \text{LN}(\mathbf{X}) \\
 \mathbf{Q}_{hw}, \mathbf{Q}_{ch}, \mathbf{Q}_{cw} &= \text{DWConv}_{3 \times 3}(\mathbf{Q}) \\
 \mathbf{X}'_{\text{queried}} &= \text{Concat}(\mathbf{Q}_{ij} \odot \mathbf{X}_{ij} \text{Conv}_{1 \times 1}(X_0)) \\
 \mathbf{X}_{\text{queried}} &= \text{MLP}(\mathbf{X}'_{\text{queried}}) + \mathbf{X}
 \end{aligned} \tag{1}$$

where $\text{LN}(\cdot)$ denotes layer normalization, $\text{DWConv}(\cdot)$ is depth-wise convolution and $i, j \in \{HW, CH, CW\}$. The MFIBA further enhances contextual information by cascading multiple MFIBs. Its structure as follows:

$$\text{MFIBA}(\mathbf{X}) = \text{Conv}_{3 \times 3}(\text{MFIB}_3(\text{MFIB}_2(\text{MFIB}_1(\mathbf{X})))) \quad (2)$$

By synergizing dynamic dimension-wise attention, multi-scale feature fusion, and lightweight operators, MFIBA establishes a theoretically grounded framework for efficient and adaptive dehazing, effectively addressing the spatiotemporal heterogeneity of real-world RS imagery without compromising computational practicality.

B. CSAM

Conventional RSID [41]–[43] methods often overlook color calibration during early decoding stages [44], limiting their effectiveness against the severe color distortions [15] induced by atmospheric scattering in real-world scenarios. To address this, we introduce CSAM, integrated across multiple decoder levels, to progressively refine haze-free features while ensuring color accuracy and structural integrity, as shown in Fig. 4.

CSAM enables progressive refinement of haze-free features through three key operations. First, *PixelShuffle* upsampling reconstructs high-resolution features, preserving channel-wise relationships. Second, a learnable color correction matrix $W_{\text{color}} \in \mathbb{R}^{3 \times C}$ transforms features via $I_{\text{fake}} = f_{\text{color}}(\text{Conv}_{1 \times 1}(X_{\text{up}}))$, where $f_{\text{color}}(\cdot)$ implements spectral compensation through matrix multiplication and bias addition. This operation simulates the inverse process of atmospheric scattering by adaptively adjusting RGB channel gains and offsets [45]. Third, the attention employs query-key-value (QKV) processing with depth-wise convolution refinement:

$$\begin{aligned} X_{\text{up}} &= U(X), \quad Q, K = \text{Conv}_{1 \times 1}(\text{LN}(X_{\text{up}})) \\ A &= \text{softmax}\left(\alpha \cdot \frac{QK^T}{\sqrt{d_k}}\right) \\ F_c &= AV + \text{DWConv}_{3 \times 3}(V) \end{aligned} \quad (3)$$

Here, $U(\cdot)$ denotes the upsampling operation. α is a learnable parameter and d_k is the dimension of the key vectors. V is the value vector and $\text{DWConv}_{3 \times 3}$ is a depth-wise separable convolution which preserves spatial details through parameter-efficient filtering, while the attention map $A \in \mathbb{R}^{H \times W \times C}$ emphasizes haze-invariant channels (e.g., near-infrared bands less affected by scattering). This dual-stream design is biologically inspired by the parvocellular pathway for color processing and magnocellular pathway for spatial acuity in human vision [46].

By hierarchically correcting coarse-to-fine spectral distortions—global color balance in early stages (e.g., sky regions) and local chromatic consistency in later stages (e.g., vegetation)—CSAM effectively mitigates nonlinear atmospheric-sensor interactions, enhancing real-world RSID performance.

C. MFAFM

Traditional RSID feature fusion methods, such as 1×1 convolutions and SKFusion [7], struggle to handle *altitude-dependent haze variations*—where haze density increases exponentially at lower altitudes—and fail to adaptively balance

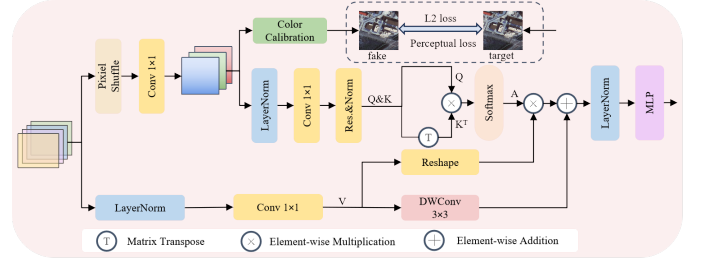


Fig. 4. Architecture of CSAM. The color calibration branch (top) learns sensor-specific spectral adjustments via W_{color} , while the attention branch (bottom) integrates global channel dependencies and local spatial details via QKV processing.

fine details (e.g., urban edges) with the global atmospheric context. Fixed-scale operators cannot jointly address these spatially heterogeneous phenomena, leading to over-smoothing or residual artifacts. The proposed MFAFM module addresses the critical challenge of multi-scale feature fusion in real-world RSID, where altitude-dependent haze density variations and complex land cover patterns demand adaptive integration of spatial-contextual information across scales. As shown in Fig. 5, the module processes three inputs: the current feature map x and two skip connections $skip1$, $skip2$ from preceding layers, each capturing distinct scale-specific characteristics.

MFAFM employs convolutional kernels of sizes 3×3 , 5×5 , and 7×7 to capture scale-specific haze patterns: small kernels preserve high-frequency details (e.g., building edges), medium kernels address mid-range gradients (e.g., vegetation clusters), and large kernels aggregate global context (e.g., sky-to-ground transitions). These operations are defined as:

$$\begin{aligned} x_1 &= \text{Conv}_{3 \times 3}(x) \\ x_2 &= \text{Conv}_{5 \times 5}(skip1) \\ x_3 &= \text{Conv}_{7 \times 7}(skip2) \end{aligned} \quad (4)$$

The resulting feature maps are then concatenated. To enhance channel-wise feature relationships, we employ a channel attention mechanism $\text{CA}(\cdot)$. Spatial relationships are further refined using a spatial attention mechanism $\text{SA}(\cdot)$:

$$\begin{aligned} X_{\text{cat}} &= \text{Concat}(x_1, x_2, x_3) \\ X_{\text{ca}} &= X \odot \text{CA}(X_{\text{cat}}) \\ X_{\text{sa}} &= X_{\text{ca}} \odot \text{SA}(X_{\text{ca}}) \end{aligned} \quad (5)$$

The refined features are then fused with the original input through residual connections. MFAFM can be summarized as:

$$\text{MFAFM}(x, skip1, skip2) = \text{Conv}_{1 \times 1}(X_{\text{sa}}) + \text{Conv}_{1 \times 1}(x) \quad (6)$$

ensuring stable gradient flow while preserving critical high-resolution details. This hierarchical fusion strategy emulates the human visual system’s multi-scale processing mechanism, where retinal ganglion cells progressively integrate local contrast and global luminance information.

D. Loss Function

MCAF-Net is optimized using a hybrid loss function combining L_2 and perceptual losses. While L_2 loss aligns predictions with ground truth for high PSNR, it may weaken

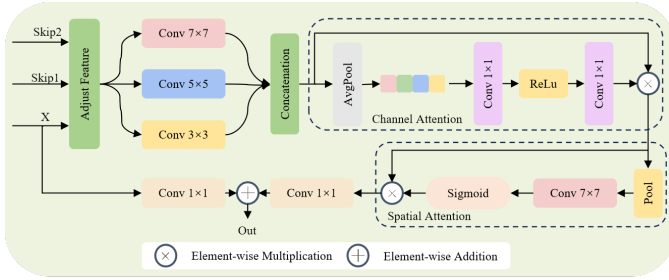


Fig. 5. Architecture of MFAFM. Three convolutional branches capture scale-specific features, while dual attention mechanisms suppress haze-corrupted components. Residual connections preserve original feature integrity.

structural similarity (SSIM). The perceptual loss, extracted from the 3rd, 8th, and 15th layers of a pretrained VGG16 network, enhances structural similarity and visual quality:

$$L_{\text{perceptual}}(\tilde{J}, J) = \sum_{l \in \{3, 8, 15\}} L_2(\text{VGG}_l(\tilde{J}), \text{VGG}_l(J)) \quad (7)$$

Perceptual loss aids in preserving the structural and detail information of the images, thereby improving the visual quality of the dehazed images. The final loss function combines these two losses, expressed as:

$$L(\tilde{J}, J) = L_2(\tilde{J}, J) + \lambda L_{\text{perceptual}}(\tilde{J}, J) \quad (8)$$

where $\lambda = 0.04$ balances the two components [9], [47].

IV. RRSRID: A REAL-WORLD RSID DATASET

RSID is a persistent challenge, particularly in real-world contexts where atmospheric conditions exhibit significant complexity and variability. Although deep learning has driven notable progress in this domain, its application to authentic RS imagery remains constrained. Studies by Li *et al.* [37] and Qin *et al.* [12] demonstrate that existing methods often falter under diverse atmospheric scattering patterns and heterogeneous scene compositions. Furthermore, Zhang *et al.* [48] underscore the limited generalization of many models to real-world RS data, attributing this to the reliance on synthetic training datasets that fail to capture the intricacies of natural haze. To bridge this critical gap, we present the Real-World Remote Sensing Hazy Image Dataset (RRSHID), a pioneering collection of 3,053 paired hazy and haze-free images. Spanning urban, agricultural, and coastal landscapes across China, these images were captured under diverse illumination and seasonal conditions. Unlike synthetic datasets such as those in [1], [7], [11], [49], which depend on simplified atmospheric models, RRSRID leverages collaborative data acquisition with meteorological agencies. This approach ensures realistic representations of altitude-dependent haze distributions and sensor-induced spectral distortions, positioning RRSRID as an essential benchmark for evaluating dehazing algorithms and advancing domain generalization in real-world RSID.

A. Image Acquisition and Processing

The development of the RRSRID involved a systematic methodology for image selection and preprocessing, implemented through collaboration with remote sensing domain

experts. Working in concert with meteorological agencies and geospatial scientists, we employed multi-temporal satellite image alignment techniques to identify spatially congruent regions captured by satellite platforms across multiple acquisition cycles. This synergistic approach enabled the acquisition of radiometrically calibrated multi-temporal image pairs exhibiting identical geographic coordinates but distinct atmospheric profiles, thereby establishing a robust dataset for real-world RSID studies.

The dataset draws from the GF_PMS: L1A optical satellite, part of the Optical and SAR Satellite Payload Retrieval system, which delivers high-resolution imagery at 1-meter panchromatic and 4-meter multispectral scales. Covering diverse terrains across China—urban centers, agricultural fields, and coastal zones—the images were acquired 2021–2023, reflecting seasonal and illumination variability. Each raw satellite image, stored in GeoTIFF format with an approximate file size of 8 GB, underwent the following preprocessing pipeline:

1) *Channel Conversion*: Multispectral images with multiple bands were transformed into 3-channel RGB (red, green, blue) format using Adobe Photoshop, prioritizing bands optimal for visual analysis.

2) *Image Cropping and Alignment*: Overlapping regions in hazy and clear image pairs were identified and cropped with precision using QGIS (Quantum Geographic Information System), selected for its advanced geospatial capabilities and scalability with large satellite datasets.

3) *Format Optimization*: Custom Python scripts further refined the cropped images, generating 256×256 -pixel subimages and converting them from TIFF to PNG format to enhance compatibility with machine learning frameworks.

B. Haze Density Estimation

To classify images by haze intensity, we adopted the dark channel prior method introduced by He *et al.* [8]. This technique estimates the transmission map $t(x)$ based on the principle that, in haze-free images, most non-sky regions exhibit at least one color channel with near-zero intensity. The dark channel is mathematically defined as:

$$J_{\text{dark}}(x) = \min_{y \in \Omega(x)} \left(\min_{c \in \{r, g, b\}} J^c(y) \right), \quad (9)$$

where J^c denotes a color channel of the haze-free image J , and $\Omega(x)$ represents a local patch centered at pixel x . The transmission map is subsequently derived as:

$$\tilde{t}(x) = 1 - \omega \min_{y \in \Omega(x)} \left(\min_c \frac{I^c(y)}{A^c} \right), \quad (10)$$

where I is the hazy image, A is the atmospheric light, and ω is a constant (typically 0.95) to retain subtle haze effects. For each image, we calculated the mean dark channel value as a proxy for haze density. Statistical analysis across the dataset established thresholds at 110.58 for thin haze and 159.31 for thick haze, as depicted in Fig. 6. Images were accordingly categorized into thin (below 110.58), moderate (110.58–159.31), and thick (above 159.31) haze levels.

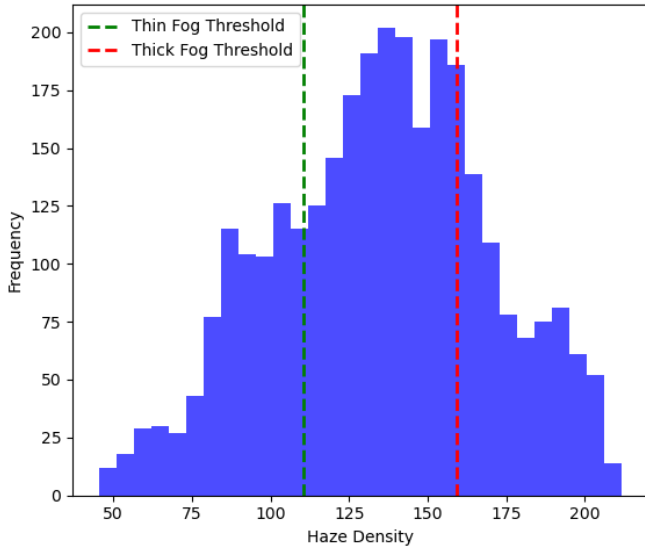


Fig. 6. Haze density distribution across the RRSIID dataset.

TABLE I
DISTRIBUTION OF IMAGE PAIRS IN THE RRSIID DATASET

Haze Level	Total	Train	Test	Validation
Thin haze	763	610	76	77
Moderate haze	1,526	1,220	152	154
Thick haze	764	611	76	77
Total	3,053	2,441	304	308

C. Dataset Characteristics

RRSHID encompasses 3,053 pairs of hazy and haze-free RS images, constituting the largest real-world dataset of its kind. These pairs are stratified by haze density into three categories, as detailed in Table I.

Each image, standardized at 256×256 pixels, strikes a balance between spatial detail and computational efficiency for deep learning applications. As the first large-scale, real-world paired RS dataset, RRSIID captures authentic atmospheric phenomena absent in synthetic counterparts, including:

- Heterogeneous haze densities and spatial distributions within individual images,
- Intricate interactions between haze and diverse land cover types (e.g., urban, vegetative, and marine),
- Natural variations in illumination and their influence on haze perception.

These properties render RRSIID a crucial resource for developing robust RSID algorithms, assessing haze impacts on applications such as object detection [50], [51] and change detection [52], [53], and deepening insights into atmospheric effects on satellite imagery.

V. EXPERIMENTS

A. Experimental Settings

1) *Datasets*: MCAF-Net is evaluated on the RRSIID dataset and four publicly available benchmarks: RSID [1], RICE1 [11], RICE2 [11] and StateHaze1K-thick [49]. These datasets are selected for their diverse characteristics:

RSID: Includes 1000 hazy and haze-free image pairs, with 900 used for training and 100 for testing.

RICE1: Comprises 500 cloudy and cloud-free pairs, split into 400 for training and 100 for testing.

RICE2: Features 736 pairs with complex thick clouds and shadows, divided into 588 for training and 147 for testing.

StateHaze1K-thick: A subset of 400 hazy pairs, allocated as 320 for training, 45 for testing, and 35 for validation.

The RRSIID dataset, designed to reflect real-world RS challenges, complements these synthetic benchmarks to assess generalization.

2) *Implementation Details*: All models trained for 300 epochs on a single NVIDIA Tesla P100-PCIE GPU. We configure the patch size to 256×256 and the batch size to 8. The Adam optimizer is utilized with $\beta_1 = 0.9$ and $\beta_2 = 0.999$, paired with an initial learning rate of 0.001, which decays to 1×10^{-8} via a cosine annealing scheduler. The network architecture comprises five stages, with embedding dimensions of [24, 48, 96, 48, 24] and corresponding depths of [8, 8, 16, 8, 8], optimizing both capacity and efficiency for RSID.

3) *Evaluation Metrics*: To assess the performance on supervised hazy datasets, we employed three metrics: Peak Signal-to-Noise Ratio (PSNR), Structural Similarity Index Measure (SSIM), and Mean Squared Error (MSE). Higher PSNR and SSIM values signify improved image quality, while lower MSE indicates enhanced dehazing efficacy.

B. Experimental Results

1) *Real-World RSID*: To evaluate MCAF-Net’s effectiveness in real-world RSID, we conducted comprehensive experiments on our RRSIID dataset. This dataset, specifically curated to represent challenging real-world scenarios, served as a robust benchmark for assessing dehazing algorithms in RS imagery.

Table II presents a detailed performance comparison of the proposed MCAF-Net against several SOTA dehazing methods on the RRSIID dataset, which encompasses real-world RS images under varying haze conditions: thin, moderate, and thick. The results, as shown in the table, indicate that MCAF-Net consistently achieves the highest performance across all haze levels and metrics, marked in red, with the second-best performances highlighted in blue.

RRSHID-thin: MCAF-Net achieves a PSNR of 23.32, an SSIM of 0.6236, and an MSE of 0.0059, surpassing all competing methods. The second-best performer, 4KDehazing [10], records a PSNR of 22.83 and an SSIM of 0.6177, trailing MCAF-Net by 0.49 in PSNR and 0.0059 in SSIM, with a higher MSE of 0.0063.

RRSHID-moderate: MCAF-Net excels with a PSNR of 23.60, an SSIM of 0.6583, and an MSE of 0.0063. In comparison, DehazeFormer [7], the second-best method, achieves a PSNR of 23.06 and an SSIM of 0.6137, falling short by 0.54 in PSNR and 0.0446 in SSIM, with an MSE of 0.0076.

RRSHID-thick: MCAF-Net demonstrates superior performance with a PSNR of 25.40, an SSIM of 0.7221, and an MSE of 0.0040. DehazeFormer obtains a PSNR of 24.69 and an SSIM of 0.7143, lagging by 0.71 in PSNR and 0.0078 in SSIM, with an MSE of 0.0051.

RRSHID-average: Across all haze levels, MCAF-Net maintains its lead with an average PSNR of 24.11, an SSIM of

TABLE II
PERFORMANCE COMPARISON OF DIFFERENT METHODS ON RRSIID DATASET ACROSS VARIOUS HAZE LEVELS. VALUES IN RED AND BLUE DENOTE THE BEST AND SECOND-BEST PERFORMANCE, RESPECTIVELY.

Method	RRSHID-thin			RRSHID-moderate			RRSHID-thick			RRSHID-average		
	PSNR	SSIM	MSE	PSNR	SSIM	MSE	PSNR	SSIM	MSE	PSNR	SSIM	MSE
DCP [8]	18.46	0.4564	0.0192	17.80	0.4856	0.0238	18.39	0.4843	0.0208	18.22	0.4754	0.0213
FFA-Net [12]	17.08	0.4452	0.0326	17.40	0.5385	0.0346	16.71	0.4792	0.0377	17.06	0.4876	0.0350
GridDehazeNet [27]	22.77	0.6145	0.0069	22.62	0.6468	0.0083	23.96	0.7112	0.0061	23.12	0.6575	0.0071
4KDehazing [10]	22.83	0.6177	0.0063	22.47	0.6505	0.0083	22.55	0.6912	0.0099	22.62	0.6531	0.0082
SCAnet [32]	18.37	0.4718	0.0200	18.11	0.0538	0.0210	19.07	0.5966	0.0180	18.52	0.3741	0.0195
Trinity-Net [1]	20.51	0.5728	0.0120	22.46	0.5728	0.0085	24.11	0.7234	0.0058	22.36	0.6230	0.0060
DehazeFormer [7]	22.74	0.6005	0.0071	23.06	0.6137	0.0076	24.69	0.7143	0.0051	23.50	0.6428	0.0066
PCSformer [31]	21.83	0.5427	0.0088	22.09	0.5984	0.0092	23.71	0.6547	0.0055	22.54	0.5996	0.0070
MCAF-Net	23.32	0.6236	0.0059	23.60	0.6583	0.0063	25.40	0.7221	0.0040	24.11	0.6680	0.0054

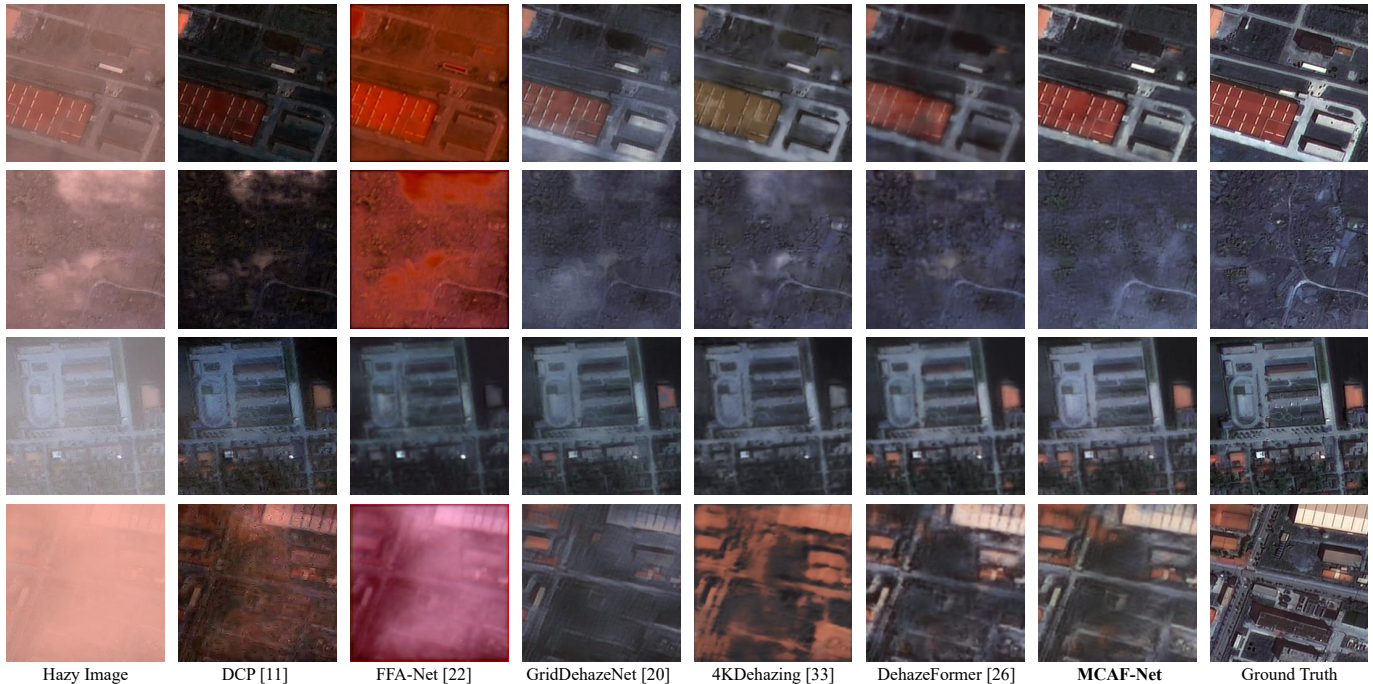


Fig. 7. Visual samples generated by the evaluated methods on the RRSIID dataset. Note that beneath each hazy or restored image, we present the corresponding error maps depicting discrepancies with the ground truth.

0.6680, and an MSE of 0.0054. The second-best results vary by metric: DehazeFormer achieves a PSNR of 23.50 (0.61 lower than MCAF-Net), GridDehazeNet [27] records an SSIM of 0.6575 (0.0105 lower), and Trinity-Net [1] yields an MSE of 0.0060 (0.0006 higher).

The consistent superiority of MCAF-Net across all haze conditions and evaluation metrics underscores its robustness and effectiveness in real-world RSID. Notably, the performance gap is most pronounced under thick haze conditions, where MCAF-Net achieves significant improvements in PSNR (0.71 higher than DehazeFormer) and MSE (0.0011 lower), indicating its capability to recover fine details and structural integrity in heavily degraded images.

Compared to established methods such as DCP [8], FFA-Net [12], SCAnet [32] and PCSformer [31], MCAF-Net demonstrates substantial improvements, especially in SSIM and MSE, reflecting its enhanced ability to preserve structural fidelity and minimize reconstruction errors. Even against more recent approaches such as GridDehazeNet, 4KDehazing, Trinity-Net, and DehazeFormer, MCAF-Net stands out as a superior solution, reinforcing its position as a SOTA method

for real-world RSID.

To provide a more comprehensive assessment beyond numerical metrics, we included visual comparisons of the dehazing results in Fig. 7. These qualitative examples offered insight into the perceptual improvements achieved by our method. Qualitative results further validate the quantitative findings, showcasing our algorithm’s ability to effectively remove haze while preserving crucial image details and enhancing overall visual clarity, while FFA-Net and Trinity-Net often leave residual haze or introduce artifacts.

In summary, the experimental results on the RRSIID dataset validate the efficacy of MCAF-Net for real-world RSID. Its consistent outperformance across diverse haze levels and metrics establishes MCAF-Net as a leading approach in this domain, offering a robust and reliable solution for enhancing the quality of haze-degraded RS imagery.

2) **Synthetic RSID**: Our method demonstrated exceptional performance in real-world RSID. To further evaluate its generalization capability, we applied the proposed approach to several publicly available synthetic RSID datasets. The methods include DCP [8], FFA-Net [12], GridDehazeNet [27],

TABLE III
PERFORMANCE COMPARISON OF DIFFERENT METHODS ON MULTIPLE HAZE DATASETS. VALUES IN RED AND BLUE DENOTE THE BEST AND SECOND-BEST PERFORMANCE, RESPECTIVELY.

Method	RSID			RICE1			RICE2			Statehaze1k-thick		
	PSNR	SSIM	MSE	PSNR	SSIM	MSE	PSNR	SSIM	MSE	PSNR	SSIM	MSE
DCP [8]	13.87	0.6892	0.0538	15.68	0.6860	0.0491	14.10	0.3898	0.0656	17.87	0.8481	0.0169
FFA-Net [12]	18.31	0.8582	0.0204	23.73	0.9068	0.0096	17.77	0.6261	0.0323	19.45	0.9023	0.0117
GridDehazeNet [27]	23.50	0.9383	0.0080	33.45	0.9766	0.0010	31.54	0.8839	0.0014	20.51	0.9097	0.0089
4KDehazing [10]	23.61	0.9415	0.0053	27.54	0.9425	0.0024	25.21	0.8604	0.0087	20.75	0.7696	0.0085
Trinity-Net [1]	23.60	0.9322	0.0060	23.46	0.8796	0.0100	18.81	0.7781	0.0200	20.43	0.8056	0.0086
PSMB-Net [28]	25.64	0.9447	0.0030	31.32	0.9444	0.0006	30.21	0.8756	0.0010	21.55	0.8489	0.0084
DehazeFormer [7]	25.04	0.9393	0.0040	36.15	0.9794	0.0005	34.54	0.8875	0.0010	22.02	0.9306	0.0063
PCSformer [31]	23.03	0.9159	0.0063	35.17	0.9564	0.0006	33.80	0.8781	0.0011	20.20	0.8125	0.0097
MCAF-Net	25.89	0.9531	0.0032	35.79	0.9814	0.0005	34.59	0.8948	0.0009	22.16	0.9308	0.0062

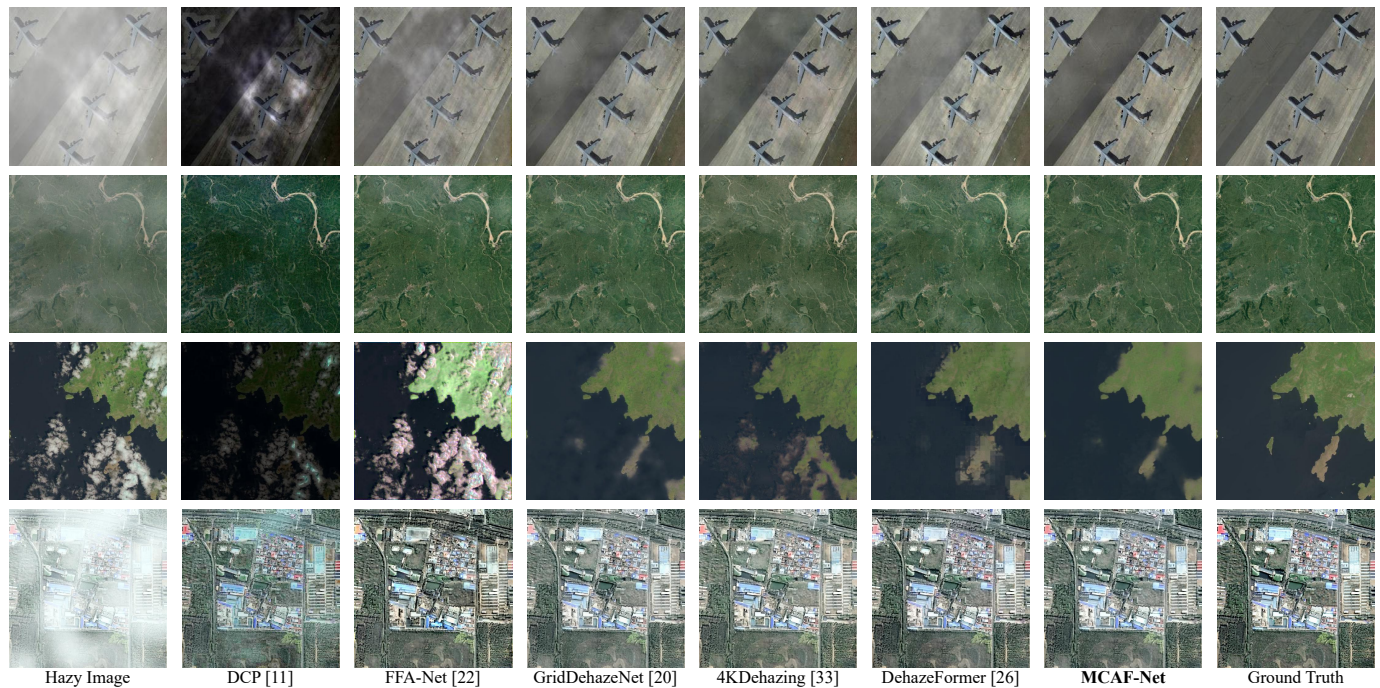


Fig. 8. Visual samples generated by the evaluated methods on RSID [1], RICE1 [11], RICE2 [11], and Statehaze1k-thick [49] datasets.

4KDehazing [10], Trinity-Net [1], PSMB-Net [28], DehazeFormer [7] and PCSformer [31] and our proposed MCAF-Net.

Theoretically, the synthetic data exhibited certain scene differences compared to the real data, which could potentially lead to suboptimal results on some public synthetic RS datasets. However, our experimental results were highly encouraging. Our method not only performed admirably on these synthetic datasets but also provided strong evidence of its robust generalization ability and resilience.

We conducted comprehensive comparative analyses across multiple SOTA methods and datasets, including RSID [1], RICE1 [11], RICE2 [11], and state1k-thick [49].

Experimental results, presented in Table III, clearly demonstrated that MCAF-Net outperformed nearly all evaluated approaches in terms of quantitative performance on synthetic RS hazy degradation datasets. Notably, our method exhibited particularly high performance in terms of SSIM scores, indicating its superiority in preserving structural information.

Visual assessments of our method alongside other evaluated approaches were illustrated in Fig. 8, further confirming the superiority of our model. These visual comparisons highlighted our method’s ability to effectively remove haze while

preserving fine details and enhancing overall image quality.

The consistent superior performance across both real-world and synthetic datasets reinforced the robustness and versatility of our proposed approach, positioning it as a promising solution for a wide range of RSID scenarios.

C. Ablation Studies

The effectiveness of the proposed modules is assessed through ablation studies conducted on the RRSID-thick dataset. These studies serve to analyze the individual contributions of each component within our proposed MCAF-Net and enable comparisons with their similar designs.

1) *Individual Components*: In this study, we employed a baseline architecture with a U-shaped design, utilizing ResNet-Block (RNB) [54] as the basic learning block. Table IV depicts the ablation on individual components. Initially, we replaced the RNB with our MFIBA, resulting in a performance gain of 0.95 dB in PSNR. Remarkably, this improvement was achieved with only 46.43% #Param and 38.65% FLOPs of the baseline model, demonstrating the efficiency and effectiveness of our MFIBA. Subsequently, incorporating our proposed CSAM module, the model achieved an additional performance

TABLE IV
ABLATION STUDY OF DIFFERENT COMPONENTS.

Model	PSNR	SSIM	MSE	#Param	FLOPs
Baseline	23.20	0.6952	0.0047	1.202M	51.28G
+MFIBA	24.15	0.7091	0.0053	558.1K	19.82G
+CSAM	24.61	0.7119	0.0045	582.3K	20.15G
+MFAFM	25.40	0.7221	0.0040	558.1K	19.82G

TABLE V
COMPARISON OF DIFFERENT BASIC LEARNING BLOCKS.

Component	PSNR	SSIM	MSE	#Param	FLOPs
RNB [54]	24.82	0.7145	0.0048	1.15M	48.56G
FNB [55]	24.95	0.7168	0.0046	892.3K	35.82G
MFIB×1	25.13	0.7196	0.0043	508.6K	18.83G
MFIB×2	25.15	0.7207	0.0044	533.3K	19.36G
MFIB×3	25.40	0.7221	0.0040	558.1K	19.82G
MFIB×4	25.19	0.7209	0.0044	571.3K	20.02G

TABLE VI
PERFORMANCE COMPARISON OF DIFFERENT COMPONENTS

Component	PSNR	SSIM	CIEDE2000	#Param	FLOPs
Baseline	23.96	0.7112	10.38	534.1K	18.50G
+ Attention	24.11	0.7234	7.37	542.3K	18.75G
+ Color Calibration	24.69	0.7143	6.27	538.5K	18.62G
+ CSAM	25.40	0.7221	5.72	558.1K	19.82G

TABLE VII
PERFORMANCE COMPARISON OF DIFFERENT FUSION MODULES

Component	PSNR	SSIM	MSE	#Param	FLOPs
1×1 Conv	25.01	0.7128	0.0045	563.1k	20.02G
SKFusion [7]	25.19	0.7132	0.0043	548.5k	19.42G
MFAFM	25.40	0.7221	0.0040	558.1K	19.82G

gain of 0.46 dB, albeit with a slight increase in computational burden (582.3K #Param and 20.15G FLOPs). This result indicated the capability of our CSAM in improving performance and demonstrated the significance of color correction in RSID. Finally, we integrated our MFAFM, which led to a substantial improvement of 0.79 dB in PSNR while maintaining similar computational efficiency as MFIBA (558.1K #Param and 19.82G FLOPs). In conclusion, the ablation studies on individual components demonstrated the significant impact of each proposed component in a positive manner.

2) *Basic Learning Blocks*: To assess the effectiveness of our proposed MFIBA, we conducted studies comparing its performance with two commonly used learning blocks, namely RNB [54] and the FasterNetBlock (FNB) [55], in the context of RSID. Table V presented the results of our experiments. Notably, our MFIB×3 outperformed RNB by a margin of 0.58 dB and FNB by a margin of 0.45 dB in terms of PSNR. Furthermore, we investigated the impact of cascading multiple MFIBs. As shown in Table V, the performance gradually improved as the number of MFIBs increases, with MFIB×3 achieving the best performance while maintaining relatively low computational cost (558.1K #Param and 19.82G FLOPs). These findings demonstrated the effectiveness of our MFIBA design and its potential for enhancing RSID performance.

3) *Capacity of CSAM*: To comprehensively evaluate the effectiveness of the CSAM, we conducted detailed ablation studies focusing on its two core components: the self-supervised color correction mechanism and the attention-guided feature refinement, with the results summarized in Table VI.

The CIEDE2000 [56] metric, which quantifies perceptual

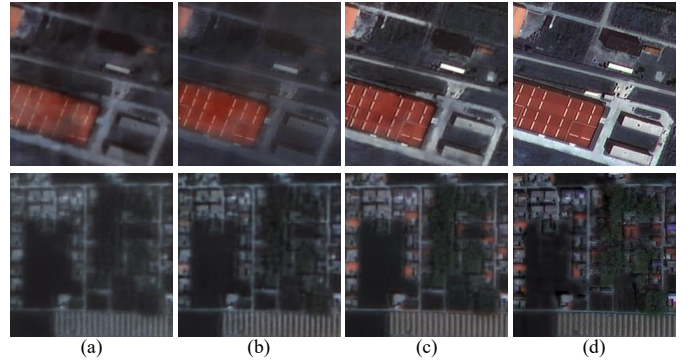


Fig. 9. Visual comparison of CSAM components: (a)+Attention, (b)+Color Calibration, (c)+CSAM, (d) Ground Truth.

TABLE VIII
PERFORMANCE COMPARISON OF DIFFERENT FUSION MODULES

Component	PSNR	SSIM	MSE	#Param	FLOPs
1×1 Conv	25.01	0.7128	0.0045	563.1k	20.02G
SKFusion [7]	25.19	0.7132	0.0043	548.5k	19.42G
MFAFM	25.40	0.7221	0.0040	558.1K	19.82G

color differences by considering luminance, chroma, and hue variations in the CIELAB color space, demonstrates progressive improvement through our component-wise analysis. When introducing the attention mechanism alone, we observe a moderate PSNR gain of 0.15 dB and SSIM improvement of 0.0122, primarily enhancing structural preservation. However, the substantial CIEDE2000 reduction from 10.38 to 7.37 (-29.0%) reveals remaining color distortion issues. The color calibration module shows complementary characteristics - it achieves the most significant CIEDE2000 improvement (6.27, -39.6% from baseline) through learnable color matrix transformation, though with slightly reduced SSIM performance due to enhanced color contrast. Our complete CSAM integration synergistically combines both advantages, delivering SOTA performance with 25.40 dB PSNR (+1.44 dB) and 5.72 CIEDE2000 (-45.0%), while maintaining practical complexity (558.1K parameters, +4.5% from baseline).

Fig 9 visually validates these findings. The attention-enhanced result (a) preserves building edges but shows yellowish haze residuals. The color-calibrated output (b) exhibits accurate sky color recovery at the expense of vegetation detail. Our full CSAM implementation (c) successfully integrates both capabilities, producing haze-free results with natural chromaticity comparable to GT (d).

These demonstrate CSAM's unique capacity to bridge the gap between synthetic training and real-world deployment in RSID tasks through physics-guided color correction and data-driven feature refinement.

4) *Adaptive Feature Fusion*: To comprehensively validate the efficacy of MFAFM, we performed systematic comparisons with two representative fusion approaches: standard 1×1 convolution and SKFusion [7]. As quantitatively demonstrated in Table VIII, the proposed MFAFM achieves marked superiority over conventional convolution operations, achieving a significant gain in PSNR of 0.39 dB. Although SKFusion marginally outperforms baseline convolution (0.12 dB improvement), our method established a new SOTA by further increasing the performance ceiling with an additional 0.21 dB enhancement.

TABLE IX
PERFORMANCE COMPARISON OF DIFFERENT LOSS FUNCTIONS.

Loss Function	PSNR	SSIM	MSE
\mathcal{L}_2	24.95	0.7217	0.0044
$\mathcal{L}_{perpetual}$	22.85	0.6873	0.0052
$\mathcal{L}_2 + \lambda\mathcal{L}_{perpetual}$	25.40	0.7221	0.0040

TABLE X
PERFORMANCE COMPARISON OF STATE-OF-THE-ART METHODS

Method	PSNR	SSIM	MSE	#Time	#Param	FLOPs
FFA-Net	16.71	0.4792	0.0377	0.1200	4.456M	287.8G
GridDehazeNet	20.24	0.6312	0.0096	0.0699	955.7K	85.72G
4KDehazing	22.55	0.6912	0.0099	0.0549	34.55M	105.8G
SCAnet	19.07	0.5966	0.0180	0.0700	2.39M	258.6G
Trinity-Net	24.11	0.7103	0.0058	0.0400	20.14M	30.78G
DehazeFormer	24.69	0.7143	0.0051	0.0831	1.205M	39.76G
PCSformer	23.71	0.6547	0.0055	0.0600	3.73M	27.66G
MCAF-Net	25.40	0.7221	0.0040	0.0498	558.1K	19.82G

This progression not only corroborated the findings in [7] but more importantly underscores MFAFM’s exceptional capability in addressing real-world RSID challenges, confirming MFAFM’s effectiveness as a multiscale adaptive paradigm for feature fusion in RSID applications.

5) *Loss Functions*: To investigate the effectiveness of different loss functions, we conducted ablation studies with various loss combinations. Table IX presented the quantitative results. Using only \mathcal{L}_2 loss achieved a PSNR of 24.95 dB. When replacing it with perpetual loss, the PSNR decreased to 22.85 dB, but showed better perceptual quality with a SSIM of 0.6873. By combining \mathcal{L}_2 and $\mathcal{L}_{perpetual}$ losses, our model achieved the best performance with a PSNR of 25.40 dB and SSIM of 0.7221, demonstrating the complementary effects of these two loss terms in optimizing both pixel-level accuracy and perceptual quality.

D. Efficiency Analysis

We conducted a comprehensive comparison of SOTA dehazing methods in Table X, evaluating their restoration quality and computational efficiency. MCAF-Net established new benchmarks for RSID by simultaneously achieving SOTA restoration quality (PSNR 25.40 dB, SSIM 0.7221) and unparalleled efficiency (558.1K parameters, 19.82G FLOPs). While Trinity-Net processes images marginally faster (0.0400s vs. 0.0498s), its PSNR lags by 1.29 dB. Compared to DehazeFormer, the prior quality leader, our method reduces the inference time by 43.9% (0.0831s vs. 0.0498s) while improving the PSNR by 0.71 dB and using 53.7% fewer parameters. This dual optimization of accuracy and resource efficiency positioned MCAF-Net as the optimal choice for real-time haze removal in resource-constrained environments.

VI. CONCLUSION AND FUTURE WORKS

In this work, we present MCAF-Net, an innovative framework for real-world RSID, designed to overcome the limitations of synthetic-to-real domain gaps through a multi-branch adaptive architecture. Our approach integrates MFIBA, CSAM, and MFAFM to achieve comprehensive feature learning, precise color restoration, and context-aware haze suppression. The introduction of the RRSID dataset—the first

large-scale real-world benchmark—provides critical support for modeling complex atmospheric variations and sensor-specific degradations. Extensive validation demonstrates that MCAF-Net not only outperforms existing methods in real-world scenarios but also maintains competitive efficiency with minimal computational overhead, offering practical value for time-sensitive earth observation tasks. While the current framework excels in static haze removal, challenges remain in handling dynamic atmospheric interactions and multi-modal sensor data. Future efforts will focus on integrating temporal modeling and cross-spectral fusion to advance toward all-weather, physics-aware RS restoration systems.

REFERENCES

- [1] K. Chi, Y. Yuan, and Q. Wang, “Trinity-net: Gradient-guided swin transformer-based remote sensing image dehazing and beyond,” *IEEE Trans. Geosci. Remote Sens.*, vol. 61, pp. 1–14, 2023.
- [2] B. Jiang, J. Wang, Y. Wu, S. Wang, J. Zhang, X. Chen, Y. Li, X. Li, and L. Wang, “A dehazing method for remote sensing image under nonuniform hazy weather based on deep learning network,” *IEEE Trans. Geosci. Remote Sens.*, vol. 61, pp. 1–17, 2023.
- [3] T. Gao, Z. Liu, J. Zhang, G. Wu, and T. Chen, “A task-balanced multiscale adaptive fusion network for object detection in remote sensing images,” *IEEE Trans. Geosci. Remote Sens.*, vol. 61, pp. 1–15, 2023.
- [4] G. Zhang, S. Lu, and W. Zhang, “Cad-net: A context-aware detection network for objects in remote sensing imagery,” *IEEE Trans. Geosci. Remote Sens.*, vol. 57, no. 12, pp. 10 015–10 024, 2019.
- [5] W. Lu, S.-B. Chen, J. Tang, C. H. Q. Ding, and B. Luo, “A robust feature downsampling module for remote-sensing visual tasks,” *IEEE Trans. Geosci. Remote Sens.*, vol. 61, pp. 1–12, 2023.
- [6] W. Lu, S.-B. Chen, Q.-L. Shu, J. Tang, and B. Luo, “Decouplet: A lightweight backbone network with efficient feature decoupling for remote sensing visual tasks,” *IEEE Trans. Geosci. Remote Sens.*, vol. 62, pp. 1–13, 2024.
- [7] Y. Song, Z. He, H. Qian, and X. Du, “Vision transformers for single image dehazing,” *IEEE Trans. Image Process.*, vol. 32, pp. 1927–1941, 2023.
- [8] K. He, J. Sun, and X. Tang, “Single image haze removal using dark channel prior,” *IEEE Trans. Pattern Anal. Mach. Intell.*, vol. 33, no. 12, pp. 2341–2353, 2010.
- [9] J. M. J. Valanarasu, R. Yasarla, and V. M. Patel, “Transweather: Transformer-based restoration of images degraded by adverse weather conditions,” in *IEEE Conf. Comput. Vis. Pattern Recog.*, June 2022, pp. 2353–2363.
- [10] B. Xiao, Z. Zheng, Y. Zhuang, C. Lyu, and X. Jia, “Single uhd image dehazing via interpretable pyramid network,” *Signal Processing*, vol. 214, p. 109225, 2024.
- [11] D. Lin, G. Xu, X. Wang, Y. Wang, X. Sun, and K. Fu, “A remote sensing image dataset for cloud removal,” *arXiv preprint arXiv:1901.00660*, 2019.
- [12] X. Qin, Z. Wang, Y. Bai, X. Xie, and H. Jia, “Ffa-net: Feature fusion attention network for single image dehazing,” *AAAI*, vol. 34, no. 07, pp. 11 908–11 915, 2020.
- [13] S. G. Narasimhan and S. K. Nayar, “Vision and the atmosphere,” *Int. J. Comput. Vis.*, vol. 48, pp. 233–254, 2002.
- [14] Y. Shao, L. Li, W. Ren, C. Gao, and N. Sang, “Domain adaptation for image dehazing,” *IEEE Conf. Comput. Vis. Pattern Recog.*, pp. 2808–2817, 2020.
- [15] M. Qin, F. Xie, W. Li, Z. Shi, and H. Zhang, “Dehazing for multispectral remote sensing images based on a convolutional neural network with the residual architecture,” *IEEE J. Sel. Topics Appl. Earth Observ. Remote Sens.*, vol. 11, no. 5, pp. 1645–1655, 2018.
- [16] D. Zhang, J. Shao, Z. Liang, X. Liu, and H. T. Shen, “Multi-branch networks for video super-resolution with dynamic reconstruction strategy,” *IEEE Trans. Circuit Syst. Video Technol.*, vol. 31, no. 10, pp. 3954–3966, 2020.
- [17] K. Zhang, W. Zuo, Y. Chen, D. Meng, and L. Zhang, “Beyond a gaussian denoiser: Residual learning of deep cnn for image denoising,” *IEEE Trans. Image Process.*, vol. 26, no. 7, pp. 3142–3155, 2017.
- [18] X. Mao, C. Shen, and Y.-B. Yang, “Image restoration using very deep convolutional encoder-decoder networks with symmetric skip connections,” *Adv. Neural Inform. Process. Syst.*, vol. 29, 2016.

- [19] S. W. Zamir, A. Arora, S. Khan, M. Hayat, F. S. Khan, and M.-H. Yang, “Restormer: Efficient transformer for high-resolution image restoration,” in *IEEE Conf. Comput. Vis. Pattern Recog.*, 2022, pp. 5728–5739.
- [20] D. Berman, T. Treibitz, and S. Avidan, “Single image dehazing using haze-lines,” *IEEE Trans. Pattern Anal. Mach. Intell.*, vol. 42, no. 3, pp. 720–734, 2018.
- [21] Q. Zhu, J. Mai, and L. Shao, “Fast single image haze removal algorithm using color attenuation prior,” in *IEEE Trans. Image Process.*, vol. 24, no. 11, 2015, pp. 3522–3533.
- [22] D. Berman, T. Treibitz, and S. Avidan, “Non-local image dehazing,” in *IEEE Conf. Comput. Vis. Pattern Recog.*, 2016, pp. 1674–1682.
- [23] B. Cai, X. Xu, K. Jia, C. Qing, and D. Tao, “Dehazenet: An end-to-end system for single image haze removal,” in *IEEE Trans. Image Process.*, vol. 25, no. 11, 2016, pp. 5187–5198.
- [24] W. Ren, S. Liu, H. Zhang, J. Pan, X. Cao, and M.-H. Yang, “Single image dehazing via multi-scale convolutional neural networks,” in *Eur. Conf. Comput. Vis.* Springer, 2016, pp. 154–169.
- [25] B. Li, X. Peng, Z. Wang, J. Xu, and D. Feng, “Aod-net: All-in-one dehazing network,” in *Int. Conf. Comput. Vis.*, 2017, pp. 4770–4778.
- [26] H. Zhang and V. M. Patel, “Densely connected pyramid dehazing network,” in *IEEE Conf. Comput. Vis. Pattern Recog.*, 2018, pp. 3194–3203.
- [27] X. Liu, Y. Ma, Z. Shi, and J. Chen, “Griddehazenet: Attention-based multi-scale network for image dehazing,” in *Int. Conf. Comput. Vis.*, 2019, pp. 7314–7323.
- [28] H. Sun, Z. Luo, D. Ren, W. Hu, B. Du, W. Yang, J. Wan, and L. Zhang, “Partial siamese with multiscale bi-codec networks for remote sensing image haze removal,” *IEEE Trans. Geosci. Remote Sens.*, vol. 61, pp. 1–16, 2023.
- [29] H. Dong, J. Pan, L. Xiang, Z. Hu, X. Zhang, F. Wang, and M.-H. Yang, “Multi-scale boosted dehazing network with dense feature fusion,” in *IEEE Conf. Comput. Vis. Pattern Recog.*, 2020, pp. 2157–2167.
- [30] Z. Chen, Y. Wang, Y. Yang, and D. Liu, “Psd: Principled synthetic-to-real dehazing guided by physical priors,” *IEEE Conf. Comput. Vis. Pattern Recog.*, pp. 7180–7189, 2021.
- [31] X. Zhang, F. Xie, H. Ding, S. Yan, and Z. Shi, “Proxy and cross-stripes integration transformer for remote sensing image dehazing,” *IEEE Trans. Geosci. Remote Sens.*, 2024.
- [32] Y. Guo, Y. Gao, W. Liu, Y. Lu, J. Qu, S. He, and W. Ren, “Scanet: Self-paced semi-curricular attention network for non-homogeneous image dehazing,” in *IEEE Conf. Comput. Vis. Pattern Recog.*, 2023, pp. 1885–1894.
- [33] L. Li, Y. Dong, W. Ren, J. Pan, C. Gao, N. Sang, and M.-H. Yang, “Semi-supervised image dehazing,” *IEEE Trans. Image Process.*, vol. 29, pp. 2766–2779, 2020.
- [34] Y. Liang, S. Li, D. Cheng, W. Wang, D. Li, and J. Liang, “Image dehazing via self-supervised depth guidance,” *Pattern Recognition*, vol. 158, p. 111051, 2025.
- [35] X. Cong, J. Gui, J. Zhang, J. Hou, and H. Shen, “A semi-supervised nighttime dehazing baseline with spatial-frequency aware and realistic brightness constraint,” in *IEEE Conf. Comput. Vis. Pattern Recog.*, 2024, pp. 2631–2640.
- [36] H. Wu, Y. Qu, J. Lin, J. Zhou, and J. Xiao, “Maxdehazenet: Multi-scale feature aggregation network with maximum flow theory for single image dehazing,” *IEEE Trans. Multimedia*, vol. 25, pp. 4876–4889, 2023.
- [37] B. Li, W. Ren, D. Fu, D. Tao, D. Feng, W. Zeng, and Z. Wang, “Benchmarking single-image dehazing and beyond,” *IEEE Trans. Image Process.*, vol. 28, no. 1, pp. 492–505, 2019.
- [38] H. Chen, Y. Wang, T. Guo, C. Xu, Y. Deng, Z. Liu, S. Ma, C. Xu, C. Xu, and W. Gao, “Pre-trained image processing transformer,” *IEEE Conf. Comput. Vis. Pattern Recog.*, pp. 12 299–12 310, 2021.
- [39] X. Glorot and Y. Bengio, “Understanding the difficulty of training deep feedforward neural networks,” *Journal of Machine Learning Research*, vol. 9, pp. 249–256, 2010.
- [40] A. G. Howard, M. Zhu, B. Chen, D. Kalenichenko, W. Wang, T. Weyand, M. Andreetto, and H. Adam, “Mobilenets: Efficient convolutional neural networks for mobile vision applications,” *arXiv preprint arXiv:1704.04861*, 2017.
- [41] S. Li, Y. Zhou, and W. Xiang, “M2scn: Multi-model self-correcting network for satellite remote sensing single-image dehazing,” *IEEE Geosci. Remote Sens. Lett.*, vol. 20, pp. 1–5, 2022.
- [42] C. Li, H. Yu, S. Zhou, Z. Liu, Y. Guo, X. Yin, and W. Zhang, “Efficient dehazing method for outdoor and remote sensing images,” *IEEE J. Sel. Topics Appl. Earth Observ. Remote Sens.*, vol. 16, pp. 4516–4528, 2023.
- [43] Y. Zheng, J. Su, S. Zhang, M. Tao, and L. Wang, “Dehaze-aggan: Unpaired remote sensing image dehazing using enhanced attention-guide generative adversarial networks,” *IEEE Trans. Geosci. Remote Sens.*, vol. 60, pp. 1–13, 2022.
- [44] Z. Liu, B. Xiao, M. Alrabeiah, K. Wang, and J. Chen, “Single image dehazing with a generic model-agnostic convolutional neural network,” *IEEE Sign. Process. Letters*, vol. 26, no. 6, pp. 833–837, 2019.
- [45] J. Yang, Q. Min, W. Lu, Y. Ma, W. Yao, and T. Lu, “An rgb channel operation for removal of the difference of atmospheric scattering and its application on total sky cloud detection,” *Atmospheric Measurement Techniques*, vol. 10, no. 3, pp. 1191–1201, 2017.
- [46] Z. Ruan, Y. Liu, G. Wen, J. Liu, Z. Hou, and Y. Zhu, “Feature distillation interaction weighting network for lightweight image super-resolution,” *AAAI*, vol. 36, no. 2, pp. 2189–2197, 2022.
- [47] T. Gao, Y. Wen, K. Zhang, J. Zhang, T. Chen, L. Liu, and W. Luo, “Frequency-oriented efficient transformer for all-in-one weather-degraded image restoration,” *IEEE Trans. Circuit Syst. Video Technol.*, 2023.
- [48] L. Zhang, L. Zhang, and B. Du, “Deep learning for remote sensing image understanding,” *Journal of Sensors*, vol. 2016, 2020.
- [49] B. Huang, L. Zhi, C. Yang, F. Sun, and Y. Song, “Single satellite optical imagery dehazing using sar image prior based on conditional generative adversarial networks,” in *IEEE Winter Conf. Appl. Comput. Vis.*, 2020, pp. 1806–1813.
- [50] W. Lu, S.-B. Chen, C. H. Q. Ding, J. Tang, and B. Luo, “Lwganet: A lightweight group attention backbone for remote sensing visual tasks,” *arXiv preprint arXiv:2501.10040*, 2025.
- [51] W. Lu, S.-B. Chen, H.-D. Li, Q.-L. Shu, C. H. Q. Ding, J. Tang, and B. Luo, “Legnet: Lightweight edge-Gaussian driven network for low-quality remote sensing image object detection,” *arXiv preprint arXiv:2503.14012*, 2025.
- [52] L. Wang, Z.-H. You, W. Lu, S.-B. Chen, J. Tang, and B. Luo, *TGRS, year = 2024, pages = 1–12, title = Attention-Aware Sobel Graph Convolutional Network for Remote Sensing Image Change Detection, volume = 62.*
- [53] T. Liu, M. Zhang, M. Gong, Q. Zhang, F. Jiang, H. Zheng, and D. Lu, “Commonality feature representation learning for unsupervised multimodal change detection,” *IEEE Trans. Image Process.*, vol. 34, pp. 1219–1233, 2025.
- [54] K. He, X. Zhang, S. Ren, and J. Sun, “Deep residual learning for image recognition,” in *IEEE Conf. Comput. Vis. Pattern Recog.*, 2016, pp. 770–778.
- [55] J. Chen, S.-h. Kao, H. He, W. Zhuo, S. Wen, C.-H. Lee, and S.-H. G. Chan, “Run, don’t walk: chasing higher flops for faster neural networks,” in *IEEE Conf. Comput. Vis. Pattern Recog.*, 2023, pp. 12 021–12 031.
- [56] M. R. Luo, G. Cui, and B. Rigg, “The development of the cie 2000 colour-difference formula: Ciede2000,” *Color Research & Application*, vol. 26, no. 5, pp. 340–350, 2001.